Defect-induced incompatibility of elastic strains: Dislocations within the Landau theory of martensitic phase transformations

R. Gröger,* T. Lookman, and A. Saxena
Theoretical Division and Center for Nonlinear Studies, Los Alamos National Laboratory, Los Alamos, New Mexico 87545, USA
(Received 17 July 2008; revised manuscript received 18 September 2008; published 3 November 2008)

In dislocation-free martensites the components of the elastic strain tensor are constrained by the Saint-Venant compatibility condition which guarantees continuity of the body during external loading. However, in dislocated materials the plastic part of the distortion tensor introduces a displacement mismatch that is removed by elastic relaxation. The elastic strains are then no longer compatible in the sense of the Saint-Venant law and the ensuing incompatibility tensor is shown to be proportional to the gradients of the Nye dislocation density tensor. We demonstrate that the presence of this incompatibility gives rise to an additional long-range contribution in the inhomogeneous part of the Landau energy functional and to the corresponding stress fields. Competition among the local and long-range interactions results in frustration in the evolving order parameter (elastic) texture. We show how the Peach-Koehler forces and stress fields for any distribution of dislocations in arbitrarily anisotropic media can be calculated and employed in a Fokker-Planck dynamics for the dislocation density. This approach represents a self-consistent scheme that yields the evolutions of both the order parameter field and the continuous dislocation density. We illustrate our method by studying the effects of dislocations on microstructure, particularly twinned domain walls, in an Fe-Pd alloy undergoing a martensitic transformation.

DOI: 10.1103/PhysRevB.78.184101 PACS number(s): 81.30.Kf, 63.70.+h, 61.72.Lk, 05.70.Fh

I. INTRODUCTION

A mesoscopic description (nano- to micrometer) of physical processes in solids, where atomic length scales merge with those of the continuum, represents a crucial and perhaps most challenging aspect of understanding material behavior. This arises, for example, during displacive (martensitic) phase transformations where the distortions associated with the strains in unit cells and intraunit cell displacements (or shuffles) propagate over larger distances so that competing long-range effects lead to the formation of inhomogeneities such as interfaces, spatially correlated domains, and complex microstructure. It is the least understood regime compared to the atomic and continuum scales because the simplifications and advantages of theory in handling small or large length scales and fast or slow time scales no longer apply. The predictions of atomistic models become typically invalid at length scales larger than about a nanometer, whereas the lack of the detailed description in continuum theories makes them inappropriate for studies of physical processes occurring at length scales below a millimeter.

Our focus will be on materials undergoing structural phase transformations that represent an important and broad class of advanced materials frequently utilized in state-of-the-art applications such as surgical tools, artificial muscle fibers, aerospace and robotic applications, and novel microelectronic devices. Examples include shape memory alloys (Ni-Ti, Fe-Pd, Au-Cd, and Cu-Al-Ni), nuclear materials (Pu and U-Nb), ferroelectrics with spontaneous polarization ($BiFeO_3$, $LuFe_2O_4$, and $LiCu_2O_2$), strain-induced ferroelectric perovskites and high-k insulators ($BaTiO_3$, $SrTiO_3$, $PbTiO_3$, and $LaAlO_3$), magnetic shape memory alloys (Fe-Pd and Ni_2MnGa), or even materials with ferrotoroidic ordering [$LiCoPO_4$ and $Co_3B_7O_{13}Br$(I)]. Related materials with additional degrees of freedom include the recently discovered single-phase multiferroics displaying magnetoelectricity ($BiMnO_3$, $TbMnO_3$, and $HoMnO_3$) where magnetization and polarization are coupled to the lattice and where noncollinear structures arise. The stable crystal structure in martensites at high temperatures, often of cubic symmetry, is identified as *austenite*. Near the transformation temperature T_c, the coordinated motion of all atoms spontaneously breaks the symmetry of the high-temperature phase and several variants of the low-temperature phase, the *martensite*, ensue. This phase is a combination of all the individual martensite variants, the fraction of which in the microstructure depends on many factors such as the ambient temperature, rate of cooling, or applied stress. The typical symmetries of the martensite include tetragonal [Fe-Pd, In-Tl, Ni-Al(Mn), Fe-Ni-C, $BaTiO_3$, and Ni_2MnGa], orthorhombic [Au-Cd, U_6Nb, Ti-Ta(Pd), Cu-Ni-Al(Ti), and U], monoclinic [Ni-Ti, Ni-Ti-Al(Cu,Fe,Mn,Pd), Cu-Al-Zn(Be), Zr_2CuCo, and Pu], or trigonal/rhombohedral [Au-Cd, Ni-Ti, Ti-Ni-Al(Fe)]. As recognized early by Landau,[1–3] an important condition for displacive phase transformations to occur is that the symmetry group of the martensite is a subgroup of the symmetry group of the austenite. The ratio between the numbers of the symmetry operations of the austenite and the martensite then determines the number of different martensite variants possible in the microstructure below T_c. For example, for a cubic-to-monoclinic phase transformation, the initial cubic symmetry is described by 48 symmetry elements, whereas the final monoclinic symmetry is described by only 4. Below T_c, the high-temperature cubic symmetry is thus spontaneously broken into 12 variants of the martensite. Because all martensite variants have the same energy, the final microstructure below T_c is typically composed of regions accommodating these individual variants. When different martensite variants are brought together to form an interface, it leads to a strain-matched or strain-free twin boundary or do-

main wall if properly oriented. Otherwise, there exist transition zones at the domain boundaries that contribute extra compressional and shear energies. It may thus be favorable for the structure to form twin boundary dislocations to lower the free energy. Similarly, a habit plane between the parent austenite and product martensite variants is an invariant strain plane if properly matched and oriented so that there is a twinned microstructure in the martensite with rapidly decaying strain fields in the austenite. Upon cooling from the austenitic phase, the individual martensite variants may form a precursor or tweedlike microstructure just above the transition temperature which then transforms into a fully twinned pattern below the transformation temperature. These morphologies have been well characterized experimentally, for example, in the $L1_0$ γ_1 phase of the intermetallic Fe-Pd,[4–6] Ni-Ti,[7,8] Au-Ti,[9] U-Nb,[10] and Cu-Zn-Al.[11]

Energy-minimizing principles are now widely employed to study equilibrium microstructure and evolution of martensitic phase transformations. The approach pioneered by Barsch and Krumhansl[12] utilizes a nonlinear free energy together with strain inhomogeneity in terms of appropriate order parameter strains that drive the transformation from austenite to martensite. The one-dimensional interface solutions were shown to be solitonlike. Part of the motivation was to demonstrate how martensite formation can be described within a continuum framework without the need to invoke dislocations. These ideas were subsequently extended to two dimensions. However, the solutions for the martensitic structure were always in terms of displacement fields[13] rather than strains. The effects of compositional fluctuations and a description of the precursor, the tweed microstructure, in Fe-Pd were considered in a Monte Carlo study of Kartha *et al.*[14] in which the free energy was written in terms of strains that contained elastic signatures associated with compositional effects. The strains were written as gradients of the displacement field and the Saint-Venant compatibility constraint served as the integrability condition for strain fields. Incorporating this constraint leads to long-range interactions in the order parameter fields and the minimum of the free energy is obtained for a twinned microstructure typical of the martensite phase. The multiscale consequences of the strain-only model were investigated by Shenoy *et al.*[15] The nature of the repulsive potential associated with the microstructure, strain order parameter dynamics, and extensions to two-dimensional ferroelastic transformations were reviewed by Lookman *et al.*[16] Applications to phase transformations in shape memory polycrystals and dynamic strain loading in martensites undergoing a cubic-to-tetragonal transformation were further studied by Ahluwalia *et al.*[17] The validity of the Saint-Venant compatibility constraint guarantees that the strain field can be obtained from a known displacement field by taking gradients. On the other hand, if one knows the strain field, the displacement field is determined up to a rigid-body motion by integration. These statements are only true when the material does not contain any topological defects. For example, if dislocations are present the displacement field becomes multivalued and its gradient, i.e., the strain field, is not defined. Hence, previous studies using a strain-only description are valid for defect-free media only.

Mesoscopic studies of the collective phenomena associated with defects have focused primarily on the mechanisms involved in dislocation pattern formation. Groma and co-workers[18–20] formulated a statistical model for the evolution of the dislocation density in isotropic bodies, where the stress field associated with each dislocation is given analytically.[21,22] For the case of single slip in two dimensions, the dislocation density evolves according to a Fokker-Planck equation in which the Peach-Koehler force[23] on each dislocation is determined from the known stress field. A different framework, based on statistical studies of dislocation patterning developed by El-Azab,[24,25] makes closer connection with the Kröner continuum theory of dislocations.[26] It not only accounts for long-range interactions between dislocations but also treats each discrete slip system separately. By calculating pair correlations between dislocations in this statistical model, Zaiser *et al.*[27] demonstrated that dislocation systems exhibit a patterning instability and this leads to the formation of dislocation walls perpendicular to the glide plane. These statistical ensembles of dislocations have been shown to exhibit intrinsic spatiotemporal fluctuations with scale-invariant characteristics, long-range correlations, and emergence of strain bursts (for a recent review, see Ref. 28). In addition, continuum theories of dislocations and self-stresses as developed by Kröner,[26] Kosevich,[29] and others have been applied to studies of dislocation patterning. Among the most prominent are the contributions of Kratochvíl and Sedláček[30] and Sedláček *et al.*[31] where the evolution of the dislocation density is formulated in both the Eulerian and the Lagrangian frames. A phase-field formulation of the dislocation patterning in isotropic media was developed by Rickman and Viñals,[32] where the dislocation density tensor is obtained by minimizing the free energy. However, this model does not include coupling between the dislocation density and the underlying crystal structure and, therefore, it does not exhibit any structural phase transition. Most recently, Roy and Acharya[33] implemented the Kröner theory to study dislocation patterning using the finite-element method (FEM). A similar approach was adopted by Limkumnerd and Sethna[34] to formulate a mesoscopic Landau theory in which the free energy is written in terms of the plastic distortion tensor. The plastic distortion field that minimizes the free energy is then used to calculate the dislocation density which plays the role of the order parameter. The added advantage of this formulation is that the same model applies to dislocation motion by pure glide and by a combination of glide and climb. Therefore, it allows for studies of dislocation patterning in isotropic materials at both low and high temperatures. However, the stress associated with individual dislocations is still calculated using the isotropic elasticity.[21,22]

Experimental studies of the interaction of martensite plates with defects have focused predominantly on the copper-based alloys, in particular Cu-Zn-Al (for review, see Ref. 35). In their transmission electron microscopy (TEM) studies of Cu-Zn-Al, Ríos-Jara and Guénin[36] and Pons *et al.*[37] observed mixed $\langle 100 \rangle$ dislocations with the line directions parallel to $\langle 111 \rangle$ and gliding on $\{110\}$ planes. This is in contrast to the TEM studies of $L1_0$-ordered Fe-Pd alloys,[6] where the plastic strain was accommodated by the glide of ordinary $1/2\langle 110 \rangle$ edge dislocations accompanied by mechanical twinning in the $\{111\}\langle 112 \rangle$ systems. Theoretical discussion of irreversibility associated with the formation of

lattice defects was given by Bhattacharya *et al.*[38] and a generic energy profile was introduced to study dislocation-assisted reconstructive transformations. Utilizing a similar potential, Pérez-Reche *et al.*[39] developed a spin model in which the reversible phase transformation is coupled with the irreversible formation of dislocations. By training the system that contains a minimum amount of preexisting dislocations, they observed nucleation and self-organization of dislocations and approach of the system to self-organized criticality. However, the model does not contain long-range elastic forces.

Theoretical descriptions of reconstructive phase transformations that are accompanied by dislocations and point defects are often thought to lie outside of the applicability of the Landau theory.[40] Our objective in this paper is to demonstrate that this is not necessarily true and that a simple model in which dislocations are incorporated into the Landau theory can be formulated. Unlike the previous studies cited above, we consider an anisotropic medium that is described by the elastic constants corresponding to the high-temperature cubic phase. Utilizing Kröner's continuum theory of dislocations,[26] we show that the presence of dislocations induces *incompatibility* between the elastic components of the strain tensor field, and this is connected to the gradients of the dislocation density. The presence of dislocations is responsible for a nonlocal coupling of the incompatibility field with the order parameter. As a consequence, the evolving martensitic texture is affected by the finite density of dislocations. Minimizing the free energy subject to the incompatibility constraint for a given distribution of dislocations generates a stress field that corresponds exactly to this distribution of defects. By inserting a single edge dislocation into an otherwise ideal crystal, we show that the order parameter field that minimizes the free energy subject to this incompatibility constraint yields the correct long-range stress field around this dislocation. The fact that the stress field in a generally anisotropic material with arbitrary distribution of dislocations can be calculated by merely minimizing the free energy means that we can easily calculate the Peach-Koehler forces that act on these individual dislocations. These forces are then used in the Fokker-Planck equation for an evolution of the dislocation density. The procedure outlined above represents a self-consistent scheme that is solved recursively. In the first step, the order parameter field is calculated by minimizing the free energy subject to the incompatibility constraint that is obtained from the given dislocation density. For the known order parameter field, the Peach-Koehler forces on individual dislocations are calculated and utilized in the evolution equation to update the dislocation density and thus also the corresponding incompatibility field.

The mesoscopic nature of our approach makes this work different from the more nanoscale-based models, in particular, the phase-field microelasticity theory of Khachaturyan[41] and Wang *et al.*[42] In their work the dislocation loops are viewed as coherent platelet inclusions that expand, interact with other loops in the same and other slip systems, and annihilate in response to their internal long-range strain fields and externally applied load. The dislocation content of each slip system is described by an integer-valued density function η that specifies the number of dislocations with prescribed direction of the Burgers vector. The total energy is written in terms of stress-free strain due to individual dislocation loops and the evolution of the order parameter field η is studied using a Langevin dynamics based on the time-dependent Ginzburg-Landau equation. This model has been successfully utilized in studies of heterogeneous nucleation of martensite in the parent austenitic matrix (for an excellent review, see Ref. 43). The martensitic embryo was shown to grow inside the dislocation loop that expands in response to the external load, giving rise to the so-called stress-induced martensite. In contrast, within the Barsch-Krumhansl formulation of martensite,[12] which is utilized in this paper, twins nucleate spontaneously by lowering the temperature and without the need for an externally applied load provided that the system contains a certain minimum degree of strain inhomogeneities induced by thermal fluctuations of the lattice. In the present work, this is no longer needed because the heterogeneous nucleation of the martensite takes place readily on preexisting dislocations.

The plan of our paper is as follows. In Sec. II we review the continuum theory of dislocations and show how we include the dislocation density as the source of the incompatibility. In Sec. III we eliminate this constraint in favor of long-range interactions in the dislocation density and its nonlocal coupling with the elastic strains. In Secs. IV and V we show how the total free energy is minimized using relaxational dynamics and how the dislocation density is evolved using the Fokker-Planck equation, respectively. In Sec. VI we utilize the theory developed in this paper to study martensitic phase transformations and dislocation patterning in single crystals of Fe-30 at. % Pd alloys. In the first case study we consider that the dislocation density is fixed and thus the free energy is minimized solely by the order parameter field. We demonstrate that the increase in the dislocation density induces long-range internal strains in the material, and these give rise to stress-induced martensite even above the temperature T_c for a defect-free material. Below T_c the morphology of the martensite changes from well-defined $\langle 110 \rangle$ twins at low dislocation density to a twin-free order parameter field at high dislocation density. In the second case we consider ideally mobile crystal dislocations. We show that below T_c the order parameter field evolves into a series of twins corresponding to the two variants of the martensite. The equilibrium dislocation density is characterized by regions of high dislocation density in which the dislocations are arranged into walls at twin boundaries, separated by regions of low dislocation density. We show that the neighboring dislocation walls are formed by opposite Burgers vectors perpendicular to the twin boundaries. These correlated domains have been observed not only in molecular dynamics and Monte Carlo simulations[19,44] but also in experiments on Ag,[45] Ni-Ti,[7] and Fe-Pd.[46]

II. CONTINUUM THEORY OF DISLOCATIONS

In order to demonstrate how the presence of defects breaks the single-valuedness of the displacement field, we will first perform the following thought experiment as proposed originally by Kröner.[26,47] Consider a macroscopic

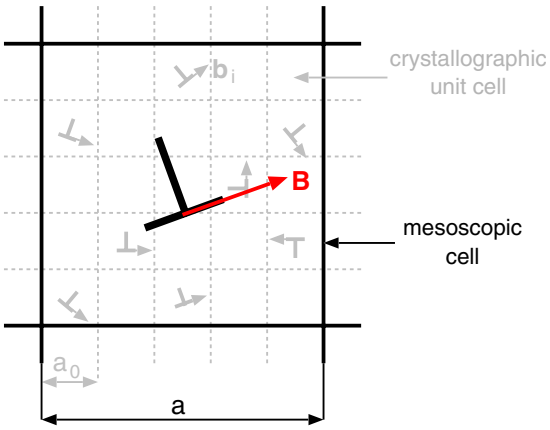

FIG. 1. (Color online) Each mesoscopic cell (solid square) is comprised of a finite number of crystallographic unit cells (dotted gray squares). The net Burgers vector $\boldsymbol{B}$ is a vector sum of the Burgers vectors of individual crystallographic dislocations (gray arrows).

single crystal whose structure belongs to a well-defined space group and its unit cell is defined by the lattice parameters $\boldsymbol{a_0}=\{a_0,b_0,c_0\}$ and angles $\boldsymbol{\alpha_0}=\{\alpha_0,\beta_0,\gamma_0\}$. Only those microscopic details associated with the crystal structure that manifest themselves at the mesoscopic level will be taken into account. This leads us to discretize the medium into a finite number of *mesoscopic* cells with lattice parameters $\boldsymbol{a}=\{a,b,c\}$ and angles $\boldsymbol{\alpha}=\{\alpha,\beta,\gamma\}$, where each such cell includes a finite number of the crystallographic unit cells. The dislocation content of each mesoscopic cell can thus be characterized by the so-called net Burgers vector $\boldsymbol{B}$ that is defined as a vector sum of the Burgers vectors $\boldsymbol{b}_i$ of the crystal dislocations in all embedded crystallographic unit cells. This is shown schematically in Fig. 1. Each of these "net dislocations",[48] characterized by its Burgers vector $\boldsymbol{B}$, causes a certain plastic distortion $\boldsymbol{\beta}^p$ that is proportional to the magnitude of $\boldsymbol{B}$. We require that the continuity of the body be maintained for any distribution of the net Burgers vectors, i.e., for any corresponding plastic distortion $\boldsymbol{\beta}^p$. In other words, by inserting dislocations in the originally defect-free medium, we are not allowed to create microcracks that would destroy the continuity of the body. This requirement is equivalent to demanding that the total distortion field $\boldsymbol{\beta}^t$ be curl-free, i.e.,

$$\nabla \times \boldsymbol{\beta}^t = \boldsymbol{0}. \tag{1}$$

Here, $\boldsymbol{\beta}^t=\boldsymbol{\beta}+\boldsymbol{\beta}^p$ is the total plastic distortion[49] that is written as a sum of its elastic part $\boldsymbol{\beta}$ and the plastic part $\boldsymbol{\beta}^p$. Each of these distortions can be expressed as a sum of their symmetric parts, i.e., strains $\boldsymbol{\varepsilon}^t$, $\boldsymbol{\varepsilon}$, and $\boldsymbol{\varepsilon}^p$, and antisymmetric parts corresponding to rotations $\boldsymbol{\omega}^t$, $\boldsymbol{\omega}$, and $\boldsymbol{\omega}^p$.

In general, two kinds of plastic distortions of a mesoscopic cell can take place depending on the way the adjacent cells are distorted; these are shown in Fig. 2. If the net Burgers vector in a given cell is the same as those in the adjacent cells, all these cells are distorted the same way and, therefore, the continuity of the body is locally preserved. Hence, $\nabla \times \boldsymbol{\beta}^p=\boldsymbol{0}$ and, with the help of Eq. (1) and $\boldsymbol{\beta}^t=\boldsymbol{\beta}+\boldsymbol{\beta}^p$, this

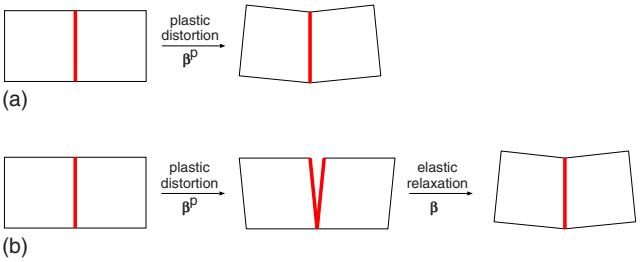

FIG. 2. (Color online) Two kinds of plastic distortions of two neighboring mesoscopic cells. The compatible plastic distortion (a) maintains the continuity of the body, while the incompatible plastic distortion (b) requires elastic relaxation to keep the body crack-free.

means that the elastic part of the strain field is also curl-free, i.e., $\nabla \times \boldsymbol{\beta}=\boldsymbol{0}$. In this case, the above-mentioned requirement of the continuous medium leads to the well-known Saint-Venant elastic compatibility constraint,[50]

$$\nabla \times \nabla \times \boldsymbol{\varepsilon} = \boldsymbol{0}. \tag{2}$$

Since the elastic strains are compatible in the sense of the Saint-Venant law, this plastic distortion is referred to as *compatible*.[51] In contrast, one can imagine a more general case where the adjacent cells are characterized by different net Burgers vectors, which means that the cells are distorted differently. Hence, the plastic part of the distortion tensor is no longer curl-free and, instead, $-\nabla \times \boldsymbol{\beta}^p=\boldsymbol{\alpha}$, where $\boldsymbol{\alpha}$ is the tensor of the density of net Burgers vectors.[52] If this plastic distortion acted alone, it would cause disregistry between neighboring mesoscopic cells[26] and thus contradiction of the requirement that we set forth by Eq. (1). However, cohesive forces of the matter act to remove this disregistry and this relaxation proceeds purely elastically. Clearly, in order to satisfy Eq. (1), the elastic strain field cannot be arbitrary but has to satisfy the constraint $\nabla \times \boldsymbol{\beta}=\boldsymbol{\alpha}$. Performing the curl of this equation and taking its symmetric part then leads to an incompatibility constraint between the components of the elastic strain tensor,

$$\nabla \times \nabla \times \boldsymbol{\varepsilon} = \boldsymbol{\eta}, \tag{3}$$

where $\boldsymbol{\eta}$ is the so-called incompatibility tensor defined as

$$\boldsymbol{\eta} = \mathrm{sym}(\nabla \times \boldsymbol{\alpha}). \tag{4}$$

In this case, the individual components of the elastic part of the strain tensor $\boldsymbol{\varepsilon}$ are not compatible in the sense of Saint-Venant law (2). Hence, this plastic distortion is called *incompatible* and the degree of this incompatibility is quantified by the symmetric tensor $\boldsymbol{\eta}$.

It is important to emphasize that since each net Burgers vector is a sum of many Burgers vectors of the underlying crystal dislocations, this coarse-graining procedure essentially determines the vector corresponding to the excess of the crystallographic Burgers vectors. Moreover, since each mesoscopic cell contains a large number of crystal dislocations, the density of net Burgers vectors can be approximated by a tensor field that is continuous throughout the entire space. In the Cartesian coordinate system with axes x_1, x_2, and x_3, this density is represented by the Nye[53] tensor α_{ij}, the

components of which relate to the net dislocations with line directions parallel to the x_i axis and the Burgers vectors parallel to the x_j axis. Hence, the diagonal elements of $\boldsymbol{\alpha}$ correspond to screw components, while the off-diagonal elements correspond to edge components of the net Burgers vectors. One can thus determine the density of the net Burgers vectors as $\alpha_{ij}=B_j/S_i$, where B_j is the jth component of the net Burgers vector and S_i are the components of the vector normal to the oriented area of the mesoscopic cell pinned by the dislocation line. The tensor α_{ij} should not be confused with the dislocation density ρ, that is, by definition, the total length of all dislocation lines that populate the medium divided by its volume.

For simplicity, consider now a two-dimensional plane strain problem in which the only nonzero components of the elastic strain tensor are ε_{11}, ε_{12}, and ε_{22}. Hence, it is straightforward to prove that the only component equation of Eq. (3) that is not identically zero is

$$\partial_{22}\varepsilon_{11} - 2\partial_{12}\varepsilon_{12} + \partial_{11}\varepsilon_{22} = \eta_{33}, \tag{5}$$

where $\partial_{ij} \equiv \partial^2/\partial x_i \partial x_j$. It is important to recognize that the scalar incompatibility field η_{33} is nonzero wherever the distribution of dislocations in the medium causes the plastic distortion to be incompatible in the sense explained above. Hence, relation (5) represents a constraint that the elastic strains have to satisfy in order to maintain the continuity of the body that has been broken locally by the incompatible plastic distortion. From Eq. (4), the incompatibility field η_{33} can be determined as

$$\eta_{33} = \partial_1 \alpha_{32} - \partial_2 \alpha_{31}, \tag{6}$$

where $\partial_i \equiv \partial/\partial x_i$. Since only the components α_{31} and α_{32} appear in this expression, only edge dislocations with their line directions parallel to x_3 and the Burgers vector components along the x_1 and x_2 axes contribute to the elastic strain incompatibility in this two-dimensional case.

In order to develop a clear link between the microscopic crystal dislocations and their coarse-grained mesoscopic manifestation by the net Burgers vector $\boldsymbol{B}$, we will now consider a finite number of discrete slip systems s. In each such system, the Burgers vector of crystal dislocations $\boldsymbol{b}^s$ is known, e.g., $\boldsymbol{b}^s = 1/2\langle 110\rangle$ (in units of the lattice parameter a_0) for edge dislocations in face-centered-cubic crystals. To each mesoscopic cell we can then attribute the net Burgers vector

$$\boldsymbol{B}(\boldsymbol{r}) = \sum_s N^s(\boldsymbol{r})\boldsymbol{b}^s, \tag{7}$$

where N^s is the number of crystal dislocations in the slip system s with the Burgers vector $\boldsymbol{b}^s$. Instead of working with integral values N^s, it is convenient to define a number density of crystal dislocations in the slip system s as $n^s = N^s/S_{\text{cell}}$, where S_{cell} is the area of a mesoscopic cell, and regard this as a continuous variable. Hence, the density of net Burgers vectors can be written as

$$\alpha_{3i}(\boldsymbol{r}) = B_i(\boldsymbol{r})/S_{\text{cell}} = \sum_s n^s(\boldsymbol{r}) b_i^s. \tag{8}$$

Substituting this expression into Eq. (6) yields the strain incompatibility in terms of the density of crystal dislocations in individual slip systems:

$$\eta_{33}(\boldsymbol{r}) = \epsilon_{ij} \sum_s \frac{\partial n^s(\boldsymbol{r})}{\partial x_i} b_j^s, \tag{9}$$

where ϵ_{ij} is the Levi-Civitá tensor. Expression (9) represents a "recipe" for coarse graining the density of crystal dislocations n^s in individual slip systems s into a continuously distributed incompatibility field η_{33}. It is important to emphasize that each slip system s contains crystal dislocations with positive and negative Burgers vectors of the same magnitude. The dislocation density n^s can thus be written as $n^s = n^{s+} - n^{s-}$, where n^{s+} and n^{s-} are non-negative densities of crystal dislocations with positive ($\boldsymbol{b}^s$) and negative ($-\boldsymbol{b}^s$) Burgers vectors, respectively. In Sec. V we will show that this distinction between positive and negative Burgers vectors of crystal dislocations is required for a systematic evolution of the dislocation density.

III. MESOSCOPIC FREE ENERGY

Consider an elastically anisotropic body of which every element is subjected to a generally nonuniform stress tensor $\boldsymbol{\sigma}$ and the response to this particular loading is characterized in each such element by the elastic strain tensor $\boldsymbol{\varepsilon}$. If we consider that a linear relation between the applied stress and induced strain applies, the free energy of this deformed medium equals the total strain energy, i.e., $F = \int_V \frac{1}{2}\sigma_{ij}\varepsilon_{ij} d\boldsymbol{r}$. Writing $\sigma_{ij} = c_{ijkl}\varepsilon_{kl}$, where c_{ijkl} is the elastic-stiffness tensor, one arrives at the free energy[54]

$$F = \int_V \frac{1}{2} c_{ijkl}\varepsilon_{ij}\varepsilon_{kl} d\boldsymbol{r}. \tag{10}$$

The elastic-stiffness tensor has generally 21 independent elastic constants but any symmetry of the underlying crystal structure reduces this number. If the stress tensor is written in the Voigt notation as $\sigma_i = [\sigma_{11}\ \sigma_{22}\ \sigma_{33}\ \sigma_{23}\ \sigma_{13}\ \sigma_{12}]^T$ and the strain tensor as $\varepsilon_j = [\varepsilon_{11}\ \varepsilon_{22}\ \varepsilon_{33}\ \varepsilon_{23}\ \varepsilon_{13}\ \varepsilon_{12}]^T$, the free energy (10) can be expressed equivalently as $F = \int_V \frac{1}{2} C_{ij}\varepsilon_i\varepsilon_j d\boldsymbol{r}$, where C_{ij} is the (6×6) symmetric elastic-stiffness matrix. For simplicity, we will be concerned in the following with cubic symmetry that is characterized by three independent elastic constants C_{11}, C_{12}, and C_{44}. The corresponding free energy then reads

$$F = \int_V \left\{ \frac{1}{2} C_{11}(\varepsilon_{11}^2 + \varepsilon_{22}^2) + C_{12}\varepsilon_{11}\varepsilon_{22} + 2C_{44}\varepsilon_{12}^2 \right\} d\boldsymbol{r}, \tag{11}$$

where we write the strains again in their usual two-index notation.

For simplicity, we will specialize in the following to the case of the square-to-rectangle phase transformations[55] that can be thought of as a two-dimensional reduction of the

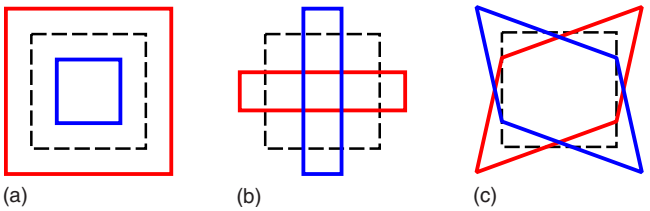

FIG. 3. (Color online) The three order parameters used to study the square-to-rectangle phase transformation in crystals of cubic symmetry: red=positive value and blue=negative value. (a) e_1, (b) e_2, and (c) e_3.

cubic-to-tetragonal (or tetragonal-to-orthorhombic) phase transformation frequently observed in shape memory alloys such as Fe-Pd, In-Tl, Ni-Al(Mn), ternary alloys Fe-Ni-C, magnetoelastic alloy Ni_2MnGa, or even perovskites such as $BaTiO_3$ that exhibit strain-induced polarization. A naive way to identify a phase transformation would be to define the order parameter as a ratio of two lattice parameters. However, this ratio alone would not distinguish between cubic and rhombohedral symmetries and, therefore, one order parameter is generally not sufficient to identify the crystal structure. In the following, we consider three scalar order parameter fields,[14]

$$e_1 = \frac{1}{\sqrt{2}}(\varepsilon_{11} + \varepsilon_{22}), \quad e_2 = \frac{1}{\sqrt{2}}(\varepsilon_{11} - \varepsilon_{22}), \quad e_3 = \varepsilon_{12}, \quad (12)$$

where e_1 measures the isotropic dilation, e_2 measures the deviatoric change in shape, and e_3 measures the change in the right angle caused by the shear. These three fundamental modes of deformation of an element in the body are shown in Fig. 3, where $e_2=0$ corresponds to the austenite and negative and positive e_2 to the two variants of the martensite. Here, e_2 serves as the primary order parameter for the square-to-rectangle transformation, whereas e_1 and e_3 are secondary order parameters. In terms of these fields, the Hookean elastic free energy, Eq. (11), for this two-dimensional problem is

$$F = \int_S \left\{ \frac{A_1}{2} e_1^2 + \frac{A_2}{2} e_2^2 + \frac{A_3}{2} e_3^2 \right\} d\boldsymbol{r}, \quad (13)$$

where the coefficients are related to the elastic constants[56] as $A_1=C_{11}+C_{12}$, $A_2=C_{11}-C_{12}$, and $A_3=4C_{44}$.

For studies of first-order phase transitions the order parameter e_2 is expanded in even powers up to the sixth order as odd powers are not allowed by symmetry. In addition, it is customary[14–16,57] to incorporate a gradient term proportional to $|\nabla e_2|^2$ that represents the energy cost for spatial variation in the order parameter, and the strain energy due to coupling of the internal strain with the externally applied stress field. Consequently, the free energy can be written as

$$F = \int_S \{ f_{\text{loc}}[e_2] + f_{\text{nonloc}}[e_1, e_3] + f_{\text{grad}}[e_2] - f_{\text{load}}[e_1, e_2, e_3] \} d\boldsymbol{r}, \quad (14)$$

where the various energy densities are

$$f_{\text{loc}}[e_2] = \frac{A_2}{2} e_2^2 + \frac{B}{4} e_2^4 + \frac{C}{6} e_2^6,$$

$$f_{\text{nonloc}}[e_1, e_3] = \frac{A_1}{2} e_1^2 + \frac{A_3}{2} e_3^2,$$

$$f_{\text{grad}}[e_2] = \frac{K_2}{2} |\nabla e_2|^2,$$

$$f_{\text{load}}[e_1, e_2, e_3] = \frac{1}{2} \sigma_{ij} \varepsilon_{ij}. \quad (15)$$

It is important to emphasize that the strain energy density as given by f_{load} applies only to the linear-elastic case, i.e., when the internal strains induced in the body by the external loading vary linearly with this applied stress.

In defect-free media the individual components of the elastic strain tensor $\boldsymbol{\varepsilon}$ are related by the Saint-Venant constraint (2). This guarantees that the strains can be determined from the known displacement field by taking its gradients. In contrast, the presence of dislocations causes discontinuities in the displacement field and, therefore, the integrability condition no longer applies. Hence, the strains are incompatible in the sense of the Saint-Venant condition and this is expressed by Eq. (3), where $\boldsymbol{\eta}$ represents the "strength" of this incompatibility. In the case of plane strain in the (x_1, x_2) plane, incompatibility constraint (5) can be expressed using Eq. (12) in terms of the order parameters as

$$\nabla^2 e_1 - (\partial_{11} - \partial_{22}) e_2 - \sqrt{8} \partial_{12} e_3 = \eta_{33} \sqrt{2}. \quad (16)$$

Now, suppose that we know the density of crystal dislocations n^s in each slip system s. Hence, the corresponding incompatibility field η_{33}, obtained from Eq. (9), is known at every point. We then seek the fields e_1, e_2, and e_3 that minimize free energy (14) subject to incompatibility constraint (16). The additive nature of the free energy allows us to perform this minimization in steps. First, we calculate the fields e_1 and e_3 that are constrained by incompatibility condition (16) and, in the second step, we obtain the primary order parameter e_2 by minimizing the free energy. The part of the free energy that depends explicitly on e_1 and e_3 reads

$$F_{13} = \int_S \{ f_{\text{nonloc}}[e_1, e_3] + f_{\text{load}}[e_1, e_2, e_3] + \lambda G[e_1, e_2, e_3, \eta_{33}] \} d\boldsymbol{r}, \quad (17)$$

where λ is the Lagrange multiplier that incorporates the incompatibility constraint $G = \nabla^2 e_1 - (\partial_{11} - \partial_{22}) e_2 - \sqrt{8} \partial_{12} e_3 - \eta_{33} \sqrt{2} = 0$. The fields e_1 and e_3 that minimize F_{13} are then obtained from the stationary conditions[58] $\delta F_{13} / \delta e_1 = 0$, $\delta F_{13} / \delta e_3 = 0$, and $\delta F_{13} / \delta \lambda = 0$. When evaluated in k-space, these conditions provide closed-form expressions for the secondary order parameter fields e_1 and e_3 in terms of the incompatibility η_{33} and the components of the externally applied stress tensor σ_{ij}:

$$e_i(\boldsymbol{k}) = Q_i(\boldsymbol{k})e_2(\boldsymbol{k}) - \sqrt{2}R_i(\boldsymbol{k})\eta_{33}(\boldsymbol{k}) - S_i(\boldsymbol{k})\sigma_{jj}(\boldsymbol{k}) - T_i(\boldsymbol{k})\sigma_{12}(\boldsymbol{k}), \quad (18)$$

where $i=1,3$. Here, $Q_1 \sim k_x^4 - k_y^4$, $Q_3 \sim k_x k_y (k_x^2 - k_y^2)$, $R_1 \sim k^2$, $R_3 \sim k_x k_y$, $S_1 \sim k^4$, $S_3 \sim k_x k_y k^2$, $T_1 \sim k_x k_y k^2$, and $T_3 \sim k_x^2 k_y^2$ are k-space kernels that we write explicitly in Appendix B, and $\sigma_{jj} = \sigma_{11} + \sigma_{22}$. Equation (18) represents the most general form[59] valid for the plane strain case in which the stress tensor has all components nonzero. With the help of Eq. (18), the nonlocal part of the free energy in Eq. (15) can be written as a functional of the primary order parameter e_2, the incompatibility η_{33}, and the components of the stress tensor σ_{ij} only:

$$f_{\text{nonloc}}(\boldsymbol{k}) = \frac{A_{13}(\boldsymbol{k})}{2}[e_2(\boldsymbol{k})]^2 - \sqrt{2}B_{13}(\boldsymbol{k})e_2(\boldsymbol{k})\eta_{33}(\boldsymbol{k}) - \Sigma_{AQ}(\boldsymbol{k})e_2(\boldsymbol{k}) + C_{13}(\boldsymbol{k})[\eta_{33}(\boldsymbol{k})]^2 + \sqrt{2}\Sigma_{AR}(\boldsymbol{k})\eta_{33}(\boldsymbol{k}) + \frac{\Sigma_A(\boldsymbol{k})}{2}, \quad (19)$$

where the k-space kernels Σ_{AQ}, Σ_{AR}, and Σ_A, written explicitly in Appendix B, depend on the external stress field. In Eq. (19), the first term represents nonlocal interactions in the e_2 field, whereas the second and third terms are couplings of e_2 with the incompatibility η_{33} and the external stress σ_{ij}, respectively. The fourth and the fifth terms are contributions from the incompatibility and its coupling to the external stress field, and the last term represents the shift in the free energy by the external stress field. If the incompatibility η_{33} vanishes and no external stress is applied, only the first term remains and we recover the nonlocal expression for an unloaded defect-free medium.[14,16]

In a similar way as we expressed f_{nonloc} in terms of e_2, η_{33}, and σ_{ij} only, we can utilize Eq. (18) to obtain a reduced expression for the strain energy density f_{load}. For plane strain, a completely general stress state leads to $f_{\text{load}} = \frac{1}{2}\sigma_{11}\varepsilon_{11} + \sigma_{12}\varepsilon_{12} + \frac{1}{2}\sigma_{22}\varepsilon_{22}$. Expressing the strains in terms of the order parameters e_1, e_2, and e_3 and using Eq. (18), one arrives at the strain energy density

$$f_{\text{load}}(\boldsymbol{k}) = W_Q(\boldsymbol{k})e_2(\boldsymbol{k}) - \sqrt{2}W_R(\boldsymbol{k})\eta_{33}(\boldsymbol{k}) - W_\Sigma(\boldsymbol{k}), \quad (20)$$

where the kernels W_Q, W_R, and W_Σ are again written explicitly in Appendix B. The remaining two free energy densities, i.e., f_{loc} and f_{grad}, are functionals of e_2 only and are determined uniquely by Eq. (15).

IV. RELAXATION OF THE PRIMARY ORDER PARAMETER FIELD

Since all constituents of the free energy are now functionals of the primary order parameter e_2, the incompatibility η_{33}, and the stress tensor σ_{ij} and assuming that the incompatibility and the external stress field change slowly relative to e_2, i.e., they remain approximately constant on the time scale of relaxation of e_2, it is straightforward to find the field e_2 that minimizes the free energy. This minimization, i.e., the solution of the equations $\delta F/\delta e_2 = 0$ and $\delta^2 F/\delta e_2^2 > 0$, cannot be performed analytically. However, we may formulate a relaxational dynamics[60] for e_2 that will follow the path of the steepest descent of the free energy F:

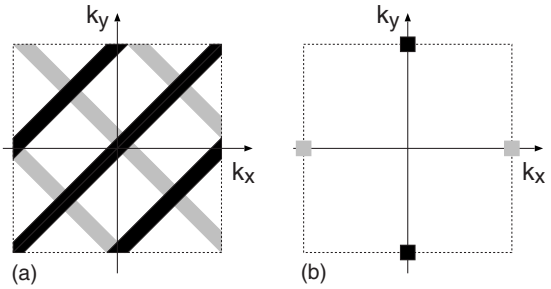

FIG. 4. Schematic illustration of the texture in e_2 that minimizes the first two terms in the nonlocal part of free energy density (19). (a) minimizes $A_{13}(\boldsymbol{k})[e_2(\boldsymbol{k})]^2$—the two orientations of twins yield the same free energy. (b) minimizes $-B_{13}(\boldsymbol{k})e_2(\boldsymbol{k})\eta_{33}(\boldsymbol{k})$—gray squares correspond to $e_2(\boldsymbol{k})\eta_{33}(\boldsymbol{k}) > 0$ and black squares to $e_2(\boldsymbol{k})\eta_{33}(\boldsymbol{k}) < 0$.

$$\frac{\partial e_2}{\partial t} = -\Gamma\frac{\delta F}{\delta e_2}, \quad (21)$$

where Γ plays the role of the mobility parameter. Writing Eq. (21) as a difference scheme, i.e., $e_2(t+\Delta t) = e_2(t) - \Delta t\Gamma\,\delta F/\delta e_2$, it is clear that Γ merely renormalizes the time step Δt. Moreover, since $\delta F/\delta e_2 = \partial(f_{\text{loc}} + f_{\text{nonloc}} + f_{\text{grad}} - f_{\text{load}})/\partial e_2$, the right-hand side of Eq. (21) can be calculated easily by taking derivatives of the previously derived free energy densities:

$$\frac{\partial f_{\text{loc}}(\boldsymbol{r})}{\partial e_2(\boldsymbol{r})} = A_2 e_2(\boldsymbol{r}) + B[e_2(\boldsymbol{r})]^3 + C[e_2(\boldsymbol{r})]^5,$$

$$\frac{\partial f_{\text{nonloc}}(\boldsymbol{k})}{\partial e_2(\boldsymbol{k})} = A_{13}(\boldsymbol{k})e_2(\boldsymbol{k}) - \sqrt{2}B_{13}(\boldsymbol{k})\eta_{33}(\boldsymbol{k}) - \Sigma_{AQ}(\boldsymbol{k}),$$

$$\frac{\partial f_{\text{grad}}(\boldsymbol{r})}{\partial e_2(\boldsymbol{r})} = -K_2\nabla^2 e_2(\boldsymbol{r}),$$

$$\frac{\partial f_{\text{load}}(\boldsymbol{k})}{\partial e_2(\boldsymbol{k})} = W_Q(\boldsymbol{k}). \quad (22)$$

If one considers a defect-free medium and no external stress is applied, the second and the third terms on the right-hand side of $\partial f_{\text{nonloc}}/\partial e_2$ vanish and also $\partial f_{\text{load}}/\partial e_2 = 0$. In this case, the nonlocal free energy density [Eq. (19)] reduces to $f_{\text{nonloc}} = [A_{13}(\boldsymbol{k})/2][e_2(\boldsymbol{k})]^2$, which is identical to the form obtained by Kartha *et al.*[14] Recognizing that the kernel $A_{13}(\boldsymbol{k}) \sim (k_x^2 - k_y^2)^2$ is minimized when $k_x = \pm k_y$, it directly follows that the system minimizes its free energy by aligning the nonzero components of the order parameter field e_2 along any of the two k-space diagonals, as shown in Fig. 4(a). The system thus develops diagonal striations in real space, similar to the tweed microstructure that is a general feature of many martensites.[4–11]

The presence of dislocations changes the evolving order parameter texture considerably and this can be demonstrated by examining the first three terms in Eq. (19). As mentioned

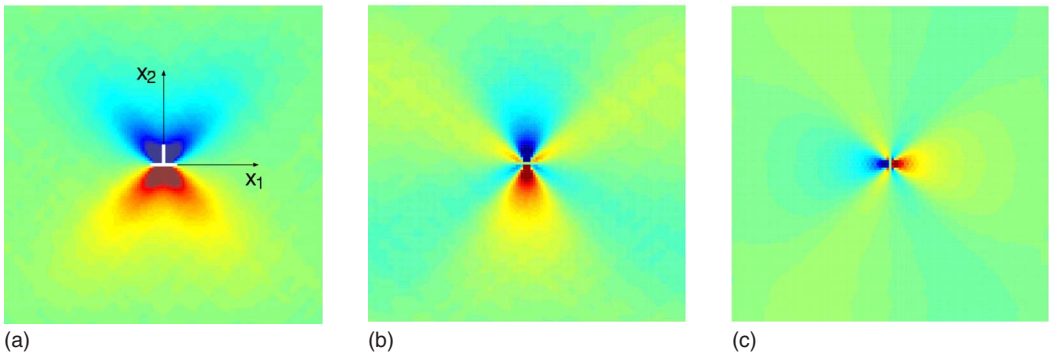

FIG. 5. (Color online) Stress field around one edge dislocation with its Burgers vector parallel to the x_1 axis (blue=negative value; red=positive value). Because periodic boundary conditions are used in this calculation, the stress field shown here corresponds to one dislocation from a periodic array of dislocations of the same kind. (a) $\sigma_{11}(\boldsymbol{r})$, (b) $\sigma_{22}(\boldsymbol{r})$, and (c) $\sigma_{12}(\boldsymbol{r})$.

above, the first term is minimized when all nonzero components of $e_2(\boldsymbol{k})$ are aligned along the k-space diagonal, as shown in Fig. 4(a). In the second term, the kernel $-B_{13}(\boldsymbol{k}) \sim -k_x^2+k_y^2$ is minimized when $\boldsymbol{k}=(\pm\pi/l,0)$ and maximized when $\boldsymbol{k}=(0,\pm\pi/l)$, where l is the real-space width of the simulated domain. Therefore, the second term in Eq. (19) is minimized when positive $e_2(\boldsymbol{k})\eta_{33}(\boldsymbol{k})$ is at the minimum of $-B_{13}(\boldsymbol{k})$, i.e., at $\boldsymbol{k}=(\pm\pi/l,0)$, and, simultaneously, negative $e_2(\boldsymbol{k})\eta_{33}(\boldsymbol{k})$ is at its maximum, i.e., at $\boldsymbol{k}=(0,\pm\pi/l)$. This is shown in Fig. 4(b). In the real space the minimum of the second term in Eq. (19) thus corresponds to a three-state "checkerboard" pattern with the periodicities along the x_1 and x_2 axes equal to twice the width of the mesoscopic cell. The size of the mesoscopic cell thus imposes an intrinsic length scale in the order parameter field. Similarly, one can identify the pattern that minimizes the third term in Eq. (19) which now depends on the external stress field. Since the first three terms in f_{nonloc} cannot be minimized simultaneously when a finite incompatibility is introduced, they naturally compete with each other. Hence, the minimization of the free energy by the field e_2 subject to a fixed distribution of dislocations is inherently frustrated and e_2 does not always evolve into a well-defined diagonal texture as it does in defect-free materials. We will see later that the diagonal texture is preferred at low dislocation densities, whereas at high dislocation densities the terms containing the incompatibility η_{33} become significant and the texture in e_2 tends to that corresponding to Fig. 4(b).

V. EVOLUTION OF THE DISLOCATION DENSITY

From the order parameter field e_2 that minimizes the free energy, we can obtain e_1 and e_3 using Eq. (18) and subsequently ε_{11}, ε_{12}, and ε_{22} using Eq. (12). Assuming linear-elastic dependence between the stresses and strains and using the three anisotropic elastic constants C_{11}, C_{12}, and C_{44}, the components of the internal stress field are obtained from

$$\begin{bmatrix} \sigma_{11}(\boldsymbol{r}) \\ \sigma_{22}(\boldsymbol{r}) \\ \sigma_{12}(\boldsymbol{r}) \end{bmatrix} = \begin{bmatrix} C_{11} & C_{12} & 0 \\ C_{12} & C_{11} & 0 \\ 0 & 0 & C_{44} \end{bmatrix} \begin{bmatrix} \varepsilon_{11}(\boldsymbol{r}) \\ \varepsilon_{22}(\boldsymbol{r}) \\ \varepsilon_{12}(\boldsymbol{r}) \end{bmatrix},$$

$$\sigma_{33}(\boldsymbol{r}) = \frac{C_{12}}{C_{11}+C_{12}}[\sigma_{11}(\boldsymbol{r})+\sigma_{22}(\boldsymbol{r})]. \tag{23}$$

Note that just by minimizing the free energy subject to the elastic strain incompatibility constraint, we obtained an internal stress field that is a superposition of the elastic stress fields of individual net dislocations. In order to demonstrate this, we show in Fig. 5 the calculated stress field around one edge dislocation in an isotropic medium with its Burgers vector along the positive x_1 direction. The overall distribution of stresses is in excellent agreement with the formulas derived from isotropic elasticity (see Ref. 21). However, in the derivation of the free energy no constraints were imposed on the anisotropy of elastic constants. Therefore, the stress fields of the dislocations in arbitrarily anisotropic media can also be calculated just by minimizing the free energy.

It is important to realize that each slip system contains crystal dislocations with positive and negative Burgers vectors and in our mesoscopic description we have to treat the densities of these dislocations separately. The explanation is provided in Fig. 6, where we show schematically two different sizes of the mesoscopic cell and the corresponding parallel slip planes (dotted lines) that pass through these cells. If the mesoscopic cell is of the same size as the crystallographic unit cell, Fig. 6(a), only one slip plane corresponding to each slip system s passes through this cell. In this case, positive and negative dislocations meeting in this cell annihilate and the only relevant quantity is the excess density n^s.

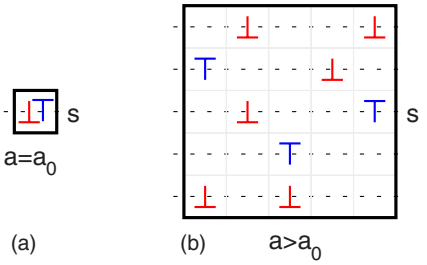

FIG. 6. (Color online) Schematic illustrations of the slip planes (dotted lines) corresponding to a particular slip system s passing through the mesoscopic cell (black square) when it comprises only one (a) and many (b) crystallographic unit cells (gray squares).

However, if the mesoscopic cell comprises a number of unit cells, shown schematically in Fig. 6(b), which is also the case in our model, several parallel slip planes pass through the cell. If we consider that the dislocations move by pure glide, the mesoscopic cell can thus contain simultaneously positive and negative dislocations in parallel slip planes and only a limited number of dislocations can annihilate. Clearly, if we are to reproduce correctly the dislocation content of the mesoscopic cell, we have to consider the densities n^{s+} and n^{s-} separately.

Without the presence of dislocation sources, the densities n^{s+} and n^{s-} of crystal dislocations in each slip system s integrated through the simulated domain must be conserved individually. This implies that the evolution equation for these dislocations densities must take the form of a continuity equation. Since we consider here that crystal dislocations move only by glide in their corresponding slip planes, the evolution equation for the dislocation densities reads

$$\frac{\partial n^{s\pm}(\boldsymbol{r},t)}{\partial t} = -D\nabla\cdot[\boldsymbol{F}^{s\pm}_{\text{glide}}(\boldsymbol{r},t)n^{s\pm}(\boldsymbol{r},t)]. \tag{24}$$

Here, $\boldsymbol{F}^{s\pm}_{\text{glide}}(\boldsymbol{r},t)$ represents the glide component of the Peach-Koehler force on the crystal dislocations with the densities $n^{s\pm}$ in the mesoscopic cell at $\boldsymbol{r}$ and time t, and can be calculated as follows. If the internal stress tensor is known at $\boldsymbol{r}$, the components of the total Peach-Koehler force on each crystal dislocation with the Burgers vector $\pm\boldsymbol{b}^s$ within the same mesoscopic cell can be calculated[21,22] as $F^{s\pm}_k = \mp\epsilon_{jk}\sigma_{jl}b^s_l$. The glide force is then determined by projecting this force into the corresponding slip plane, i.e., $\boldsymbol{F}^{s\pm}_{\text{glide}} = (\boldsymbol{F}^{s\pm}\cdot\boldsymbol{e}^{s\pm})\boldsymbol{e}^{s\pm}$, where $\boldsymbol{e}^{s\pm}=\boldsymbol{b}^{s\pm}/|\boldsymbol{b}^{s\pm}|$. The dislocation densities can then be updated using Eq. (24). For each slip system s the fields n^{s+} and n^{s-} then enter Eq. (9) to calculate the incompatibility field η_{33}. One can thus recalculate the order parameter e_2 that minimizes free energy (14) subject to this updated distribution of incompatibilities. The calculation is regarded as complete when the free energy is minimized by the field e_2 and, simultaneously, the corresponding stress field does not induce significant changes in the dislocation densities n^{s+} and n^{s-}. This process thus represents a self-consistent procedure for the simultaneous evolution of the primary order parameter field e_2 and of the densities of crystal dislocations in individual slip systems.

VI. SIMULATIONS

The material considered in these simulations is the shape memory alloy single crystal of Fe-30 at. % Pd for which the temperature dependence of the elastic constants, measured by Muto *et al.*,[61] is parametrized together with other coefficients entering the free energy functional in Appendix C. In our calculations the orientation of the crystal is chosen such that the x_1 axis coincides with the [100] direction, and the x_2 axis is parallel to the [010] direction. Each mesoscopic cell is characterized by 1000×1000 crystallographic unit cells with the lattice parameter $a_0=3.8$ Å. Hence the width of each mesoscopic cell is $a=0.38$ μm and its area $S_{\text{cell}} \approx 0.14$ μm^2. The initial values of the order parameter e_2 in each mesoscopic cell are drawn randomly from a uniform distribution with limits $\langle -0.04, 0.04\rangle$ which include the values of e_2 that correspond to the minima of f_{loc} below T_c. The simulated two-dimensional domain contains 128×128 mesoscopic cells with periodic boundary conditions that are automatically imposed by the k-space calculations. The width of the simulated domain is 48.64 μm. For simplicity, no external stress is applied in any simulation. The minimization of the free energy is regarded as complete when $\delta F/\delta e_2$ in Eq. (21) becomes less than 0.001 $\text{eV}/\text{Å}^3$.

The TEM observations of dislocations in polytwinned Fe-Pd thin foils by Xu *et al.*[6] reveal that the active mode accommodating plastic strain in this material is due to the glide of $1/2\langle110\rangle$ dislocations. Hence, in our two-dimensional simulations we will consider only two slip systems s, populated by crystal dislocations with Burgers vectors $\boldsymbol{b}^{1\pm}=\pm1/2[110]$ and $\boldsymbol{b}^{2\pm}=\pm1/2[\bar{1}10]$. Each mesoscopic cell is initially assigned finite densities of these crystal dislocations, n^{s+} and n^{s-}, each of which is chosen at random from a uniform distribution between 0 and $n_{\max}$, where $n_{\max}$ is varied to arrive at different dislocation densities. For each simulation the actual dislocation density ρ is given below.

A. Martensitic texture as a function of the density of dislocations

We first study the distribution of the order parameter e_2 that minimizes free energy (14): (i) in dislocation-free material and (ii) subjected to fixed dislocation density. Three finite densities of crystal dislocations are considered, given by $\rho=\{6\times10^{14}, 10^{15}, 8\times10^{15}\}$ m^{-2}. Free energy (14) is then minimized subject to the distribution of incompatibilities η_{33} that are derived from the given dislocation density using Eq. (9). No evolution of the dislocation density is allowed in this case which corresponds to a hypothetical situation where all dislocations are immobile. This minimization is performed for the temperatures both above T_c, where the austenite is stable in the defect-free medium, and below T_c, where the martensite is the stable phase.

In Fig. 7 we show how the order parameter field e_2 that minimizes free energy (14) changes as a function of the density of dislocations. The upper row corresponds to the temperature above T_c, whereas the lower row corresponds to the temperature below T_c. Above T_c, the system is progressively driven away from its free energy minimum ($e_2=0$) with increasing dislocation density ρ. This results in stabilization of the martensitic phase above T_c and the order parameter field e_2 without a well-defined texture [Figs. 7(b)–7(d)]. Below T_c, the twinned microstructure that minimizes the free energy in dislocation-free materials changes at finite densities of dislocations as a consequence of the competition between the first two terms on the right-hand side of Eq. (19). For low densities ρ, the first term dominates and the order parameter field e_2 is characterized by a twinned microstructure. With increasing dislocation density, the second term in Eq. (19) be-

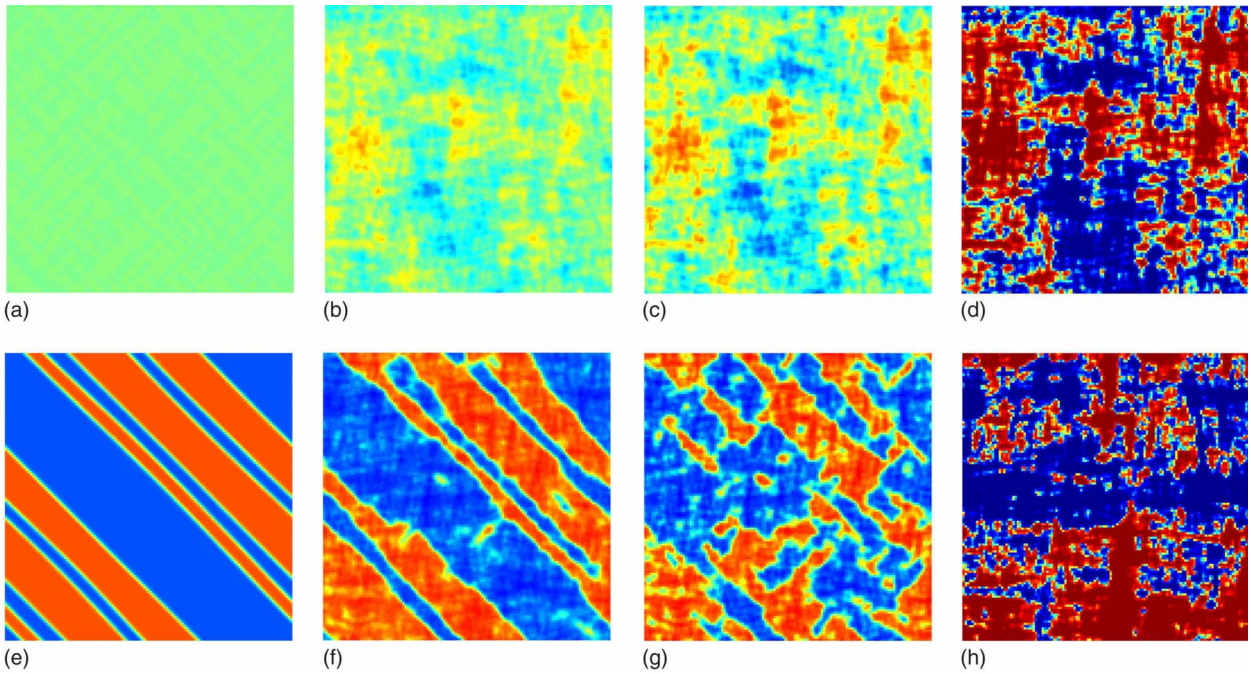

FIG. 7. (Color online) Distribution of the order parameter field $e_2(\boldsymbol{r})$ above (a–d) and below (e–h) T_c for dislocation-free medium as a function of the density of dislocations: (a,e) no dislocations, (b,f) $\rho=6\times10^{14}$ m^{-2}, (c,g) $\rho=10^{15}$ m^{-2}, and (d,h) $\rho=8\times10^{15}$ m^{-2}.

comes of the same order as the first and this competition gradually causes elimination of the twins [Figs. 7(f)–7(h)]. For large dislocation densities, i.e., Figs. 7(d) and 7(h), the strain incompatibility η_{33} completely dominates the minimization of the free energy and the same martensitic texture is obtained both above and below T_c for the defect-free medium. These results are consistent with our previous observations that dislocations alter the character of the martensitic texture (see Fig. 4).

Recall that the results shown in Fig. 7 correspond to a highly idealized case where all dislocations are immobile and the dislocation density thus cannot evolve in response to changes in the order parameter field. In the following example, we remove this constraint to simultaneously evolve the order parameter field and the dislocation density to provide a clearer picture of dislocation pattern formation below T_c.

B. Formation of dislocation walls at twin boundaries

The initial distribution of the order parameter field above and below T_c was obtained by minimizing the free energy for a dislocation-free material. In each mesoscopic cell, the two directions of the Burgers vectors in both slip systems s were then assigned randomly a dislocation density between 0 and $n_{\max}=10^{14}$ m^{-2} which yields an actual dislocation density $\rho=2\times10^{14}$ m^{-2}. We then calculated the order parameter field that corresponds to the given initial distribution of dislocations. This e_2 field is used to update the dislocation density using Eq. (24) where all dislocations have the same mobility; i.e., D is the same for the evolution of all densities $n^{s\pm}$. Since no external stress is applied, the evolution of the dislocation density is driven entirely by the evolving martensitic texture and the long-range interactions between dislocations.

Above T_c the order parameter field e_2 is close to zero everywhere and the corresponding dislocation density is spatially uniform. Below T_c the field e_2 is represented by a series of twins corresponding to the two variants of martensite [see Fig. 8(a)]. As can be seen from Fig. 8(b) the scalar density of net Burgers vectors, $|\boldsymbol{B}(\boldsymbol{r})|=\sqrt{B_1(\boldsymbol{r})^2+B_2(\boldsymbol{r})^2}$, corresponding to the minimum of the free energy, is characterized by twin boundary dislocations with the Burgers vectors parallel to the [110] and $[\bar{1}\bar{1}0]$ directions. Hence, the twin boundaries are decorated by dislocation walls with the net Burgers vectors parallel to the $\langle110\rangle$ direction, as shown in the inset of Fig. 8(b). This results in the formation of alternating positive and negative dislocation walls along the twin boundaries. Since all $\langle110\rangle$ twins have the same energy, the free energy can also be minimized by forming the 45° (rather than 135°) texture in e_2 (not shown here). In this case, the other two types of crystal dislocations, with Burgers vectors $1/2[1\bar{1}0]$ and $1/2[\bar{1}10]$, would form the dislocation walls at the twin boundaries.

VII. CONCLUSIONS

This paper introduces a simple model in which Kröner's continuum theory of dislocations[26] is incorporated into the Landau-Ginzburg theory to formulate a mesoscopic model of martensitic phase transformations mediated by plasticity. In this framework the presence of dislocations induces incompatibility between the components of the elastic strain tensor and, therefore, the Saint-Venant condition no longer applies

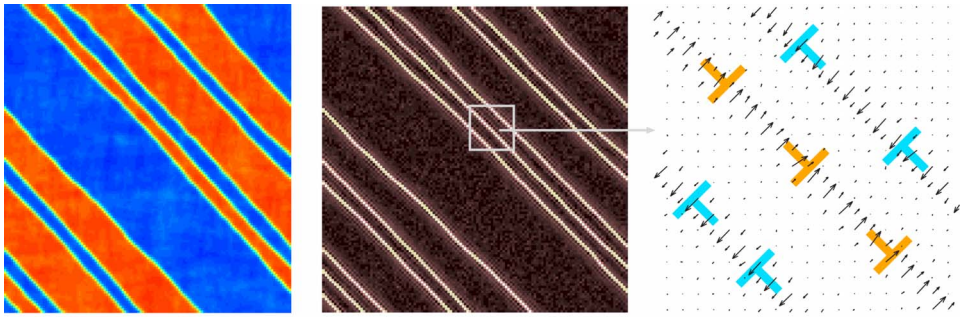

FIG. 8. (Color online) The order parameter field e_2 (a) and the distribution of the magnitudes of net Burgers vectors $|\boldsymbol{B}|$ (b) that minimize free energy (14). The blue and red regions in (a) are the two variants of the martensite, while the twin boundaries correspond to the austenite phase. In (b) the bright spots correspond to regions of high dislocation density and the dark spots correspond to low dislocation density. The inset of (b) shows the orientations of net Burgers vectors in the region marked by the gray square.

in media with defects. Instead, the elastic strains are related by an incompatibility constraint and the strength of this incompatibility is proportional to the gradients of the components of the Nye dislocation density tensor.[53] This incompatibility can be written in terms of densities of crystal dislocations in individual discrete slip systems, which provides a clear recipe for coarse graining microscopic information to the mesoscopic description. The incompatibility field is then completely determined. Moreover, we have shown that its existence leads to such interesting phenomena as the dependence of the order parameter texture on the density of dislocations or formation of correlated dislocations walls along the twin boundaries below T_c.

The presence of dislocations, i.e., the existence of a finite incompatibility field, introduces new contributions to the free energy functional, in particular coupling of the order parameter with the incompatibility field and with the applied stress tensor. We have shown that the free energy minimum cannot be reached by minimizing independently all terms that depend on the order parameter. During this minimization the coupling between the order parameter and the incompatibility field introduces competition between these terms and the minimization of the free energy is thus inherently frustrated by the finite dislocation density. The order parameter field that minimizes the free energy subject to a given distribution of dislocations (i.e., strain incompatibilities) can be directly used to calculate internal strain and stress fields. For an arbitrarily anisotropic material, one can thus obtain the Peach-Koehler forces on the dislocations just by minimizing the free energy. These forces have been employed in the evolution equations for the density of individual variants of crystal dislocations (n^{s+} and n^{s-}) which take the form of the Fokker-Planck equation. Hence, the conservation of the total Burgers vector is automatically satisfied. This procedure represents a simple self-consistent scheme in which the order parameter field is first calculated by minimizing the free energy subject to a given distribution of strain incompatibilities, i.e., densities of crystal dislocations. The corresponding internal stress field and the Peach-Koehler forces are then used to update the dislocation density using the discretized version of the Fokker-Planck equation. The new distribution of strain incompatibilities that correspond to the updated dislocation density is used again to minimize the free energy and this in turn provides the new order parameter field.

To demonstrate the main features of the model developed in this paper, we considered two case studies that represent the limits of the theory with regard to the mobility of the dislocations. In the first case the four crystal dislocations with the $1/2\langle 110\rangle$ Burgers vectors were considered as immobile and, therefore, the free energy was subject to a fixed distribution of strain incompatibilities and minimized purely by the order parameter field e_2. We have shown that the nucleation of martensite and its spatial distribution depends on the density of dislocations. At low dislocation densities the minimization of the free energy is only weakly affected and the corresponding microstructure below T_c is represented by martensite twins along the $\langle 110\rangle$ directions. In contrast, at high dislocation densities the distribution of strain incompatibilities strongly affects the minimization of the free energy and eliminates the twinned microstructure. In the second case study we considered that all dislocations are completely mobile. We have demonstrated that below T_c the free energy is minimized by forming alternating net dislocation walls at the mesoscale that decorate the twin boundaries between different variants of the martensite. The results are qualitatively consistent with the observations of correlated dislocation domains along twin boundaries in Ag,[45] Ni-Ti,[7] and Fe-Pd.[46]

Our objective here was mainly to demonstrate how the continuum theory of dislocations[26] can be incorporated into the mesoscopic free energy functional for displacive phase transformations[14] which inevitably led to a number of simplifications. Many crystallographic details are beyond the resolution of the model and thus are included only in a coarse-grained manner. In particular, short-range interactions between crystal dislocations are replaced by continuous dislocation density fields n^{s+} and n^{s-} that correspond to the two directions of the Burgers vector in the slip system s. The individual slip systems are assumed to be independent of each other and no reactions between dislocations moving in different slip planes are incorporated. No upper limit on the density of dislocations due to a finite minimum distance between dislocations of the same type is imposed at this point. Since no external loading is applied here, we do not consider the existence and operation of dislocation sources.

In the future, the model developed in this paper will be advanced to study the effect of dislocations on strain hardening and hysteresis, both of which play crucial roles in

shape memory alloys. It serves as the basis for analytical solutions of elastic fringing fields at habit planes in the presence of dislocations and thus allows for a study of the role of defects on the size dependence of the twinning width in martensites. The concept of the defect-induced incompatibility of elastic strains is general and the approach described in this paper may be applied to other phase transitions that are mediated by defects. Examples include the study of strain-induced polarization in ferroelectrics, strain-induced magnetization in ferromagnets, or even the effect of long-range strain fields of dislocations on the recently discovered ferrotoroidal ordering[62] in ferrotoroidic materials.

ACKNOWLEDGMENTS

The authors thank F.-J. Pérez-Reche, R. Ahluwalia, K. Dayal, S. Sengupta, J. San Juan, and A. Roytburd for their comments and stimulating discussion of this work during the International Conference on Martensitic Transformations (ICOMAT-08) in Santa Fe, New Mexico. In addition, they thank A. Acharya for bringing to their attention his work on the subject.

APPENDIX A: TENSORIAL REPRESENTATIONS

For convenience, the following are tensorial representations of the operations that are used throughout this paper.[63] Here, ϵ_{ijk} is the antisymmetric Levi-Civitá tensor and $\boldsymbol{A}$ is a tensor of rank two,

$$\text{divergence:} \quad \nabla \cdot \boldsymbol{A} = A_{ij,i},$$

$$\text{curl:} \quad \nabla \times \boldsymbol{A} = \epsilon_{imn} A_{jn,m},$$

$$\text{symmetric curl:} \quad \text{sym}(\nabla \times \boldsymbol{A}) = \frac{1}{2}(\epsilon_{imn} A_{jn,m} + \epsilon_{jmn} A_{in,m}),$$

$$\text{incompatibility:} \quad \nabla \times \nabla \times \boldsymbol{A} = \epsilon_{irs} \epsilon_{jmn} A_{sn,mr}.$$

APPENDIX B: k-SPACE KERNELS

In the following we write explicitly all the k-space kernels that are used to calculate the free energy and to perform the relaxational dynamics for the order parameter e_2. The denominators in these kernels are identical and we evaluate them separately as

$$d(\boldsymbol{k}) = \frac{1}{A_1} k^4 + \frac{8}{A_3} k_x^2 k_y^2. \tag{B1}$$

The following kernels are used to calculate the secondary order parameter fields e_1 and e_3 from the known primary order parameter field e_2, the incompatibility field η_{33}, and the external stress field σ_{ij}:

$$Q_1(\boldsymbol{k}) = \frac{1}{A_1} \frac{k_x^4 - k_y^4}{d(\boldsymbol{k})}, \quad Q_3(\boldsymbol{k}) = -\frac{\sqrt{8}}{A_3} \frac{k_x k_y (k_x^2 - k_y^2)}{d(\boldsymbol{k})},$$

$$R_1(\boldsymbol{k}) = \frac{1}{A_1} \frac{k^2}{d(\boldsymbol{k})}, \quad R_3(\boldsymbol{k}) = -\frac{\sqrt{8}}{A_3} \frac{k_x k_y}{d(\boldsymbol{k})},$$

$$S_1(\boldsymbol{k}) = \frac{1}{A_1 \sqrt{8}} \left[\frac{1}{A_1} \frac{k^4}{d(\boldsymbol{k})} + 1 \right], \quad S_3(\boldsymbol{k}) = -\frac{1}{A_1 A_3} \frac{k_x k_y k^2}{d(\boldsymbol{k})},$$

$$T_1(\boldsymbol{k}) = -\frac{\sqrt{8}}{A_1 A_3} \frac{k_x k_y k^2}{d(\boldsymbol{k})}, \quad T_3(\boldsymbol{k}) = \frac{1}{A_3} \left[\frac{8}{A_3} \frac{k_x^2 k_y^2}{d(\boldsymbol{k})} - 1 \right]. \tag{B2}$$

The nonlocal part of the free energy density, f_{nonloc}, and its partial derivative $\partial f_{\text{nonloc}} / \partial e_2$ are expressed using

$$A_{13}(\boldsymbol{k}) = \frac{(k_x^2 - k_y^2)^2}{d(\boldsymbol{k})}, \quad B_{13}(\boldsymbol{k}) = \frac{k_x^2 - k_y^2}{d(\boldsymbol{k})}, \quad C_{13}(\boldsymbol{k}) = \frac{1}{d(\boldsymbol{k})}. \tag{B3}$$

The kernels that depend on the above and the applied stress tensor are

$$\Sigma_{AQ}(\boldsymbol{k}) = A_1 Q_1(\boldsymbol{k}) m_1(\boldsymbol{k}) - A_3 Q_3(\boldsymbol{k}) m_3(\boldsymbol{k}),$$

$$\Sigma_{AR}(\boldsymbol{k}) = A_1 R_1(\boldsymbol{k}) m_1(\boldsymbol{k}) - A_3 R_3(\boldsymbol{k}) m_3(\boldsymbol{k}),$$

$$\Sigma_A(\boldsymbol{k}) = A_1 [m_1(\boldsymbol{k})]^2 + A_3 [m_3(\boldsymbol{k})]^2, \tag{B4}$$

where

$$m_1(\boldsymbol{k}) = S_1(\boldsymbol{k}) \sigma_{jj}(\boldsymbol{k}) - T_1(\boldsymbol{k}) \sigma_{12}(\boldsymbol{k}),$$

$$m_3(\boldsymbol{k}) = S_3(\boldsymbol{k}) \sigma_{jj}(\boldsymbol{k}) - T_3(\boldsymbol{k}) \sigma_{12}(\boldsymbol{k}). \tag{B5}$$

Here, the subscripts of each Σ imply which combination of the coefficients A_i, Q_i, R_i is used, and $\sigma_{jj} = \sigma_{11} + \sigma_{22}$.

Finally, the strain energy density f_{load} is expressed using the kernels that depend only on the applied stress tensor σ_{ij} as

TABLE I. Temperature scaling of the elastic constants and the coefficients used in free energy (14). Units: T [K], C_{ij} [GPa], and A_i [GPa].

$C_{11}(T)$	$C_{12}(T)$	$C_{44}(T)$
$104.82+0.1279T$	$229.09-0.3321T$	$71.73+0.0010T$
$A_1(T)$	$A_2(T)$	$A_3(T)$
$333.91-0.2042T$	$-124.27+0.4600T$	$282.00+0.0344T$

$$W_Q(\boldsymbol{k}) = \frac{1}{\sqrt{8}}\{[Q_1(\boldsymbol{k})+1]\sigma_{11}(\boldsymbol{k}) + [Q_1(\boldsymbol{k})-1]\sigma_{22}(\boldsymbol{k})\} + Q_3(\boldsymbol{k})\sigma_{12}(\boldsymbol{k}),$$

$$W_R(\boldsymbol{k}) = \frac{1}{\sqrt{8}}R_1(\boldsymbol{k})\sigma_{jj}(\boldsymbol{k}) + R_3(\boldsymbol{k})\sigma_{12}(\boldsymbol{k}),$$

$$W_\Sigma(\boldsymbol{k}) = \frac{1}{\sqrt{8}}\sigma_{jj}(\boldsymbol{k})m_1(\boldsymbol{k}) - \sigma_{12}(\boldsymbol{k})m_3(\boldsymbol{k}). \quad \text{(B6)}$$

APPENDIX C: TEMPERATURE DEPENDENCE OF THE ELASTIC CONSTANTS FOR Fe-30 at. % Pd

The temperature dependence of the elastic constants of Fe-30 at. % Pd alloy, measured by Muto *et al.*[61] and shown in Fig. 9, is approximated by linear relations given in Table I.

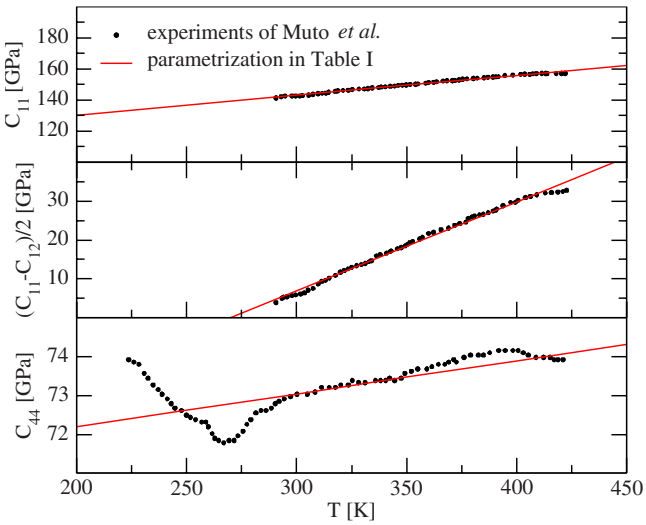

FIG. 9. (Color online) Temperature scaling of elastic constants for Fe-30 at. % Pd from Table I compared with the experimental data of Muto *et al.* (Ref. 61).

The scaling laws are obtained by fitting the experimental data for C_{11}, $(C_{11}+C_{12}+2C_{44})/2$, and $(C_{11}-C_{12})/2$ that are linear within the range of temperatures considered in these measurements. The remaining parameters B, C, and K_2 are taken from Ref. 14 and are assumed to be independent of temperature: $B=-1.7\times10^4$ GPa, $C=3\times10^7$ GPa, and $K_2/a^2=25$ GPa.

*groger@lanl.gov

[1] L. Landau, Nature (London) **138**, 840 (1936).
[2] L. Landau, Phys. Z. Sowjetunion **11**, 26 (1937).
[3] L. Landau, Phys. Z. Sowjetunion **11**, 545 (1937).
[4] G. M. Gushchin, A. A. Kuranov, F. N. Berseneva, and B. P. Adrianovskiy, Phys. Met. Metallogr. **58**, 155 (1984).
[5] B. A. Greenberg, N. A. Kruglikov, L. A. Rodionova, A. Y. Volkov, L. G. Grokhovskaya, G. M. Gushchin, and I. N. Sakhanskaya, Platinum Met. Rev. **47**, 46 (2003).
[6] D.-S. Xu, J.-P. Chang, J. Li, R. Yang, D. Li, and S. Yip, Mater. Sci. Eng., A **387-389**, 840 (2004).
[7] H. Sehitoglu, R. Hamilton, D. Canadinc, X. Y. Zhang, K. Gall, I. Karaman, Y. Chumlyakov, and H. J. Maier, Metall. Mater. Trans. A **34**, 5 (2003).
[8] S. Daly, G. Ravichandran, and K. Bhattacharya, Acta Mater. **55**, 3593 (2007).
[9] T. Inamura, R. Tachi, K. Wakashima, and H. Hosoda, in *Advanced intermetallic-based alloys*, edited by J. Wiezorek, C. L. Fu, M. Takeyama, D. Morris, and H. Clemens, MRS Symposia Proceedings No. 980 (Materials Research Society, Warrendale, PA, 2007), 0980-ll04-12.
[10] R. D. Field, D. J. Thoma, P. S. Dunn, D. W. Brown, and C. M. Cady, Philos. Mag. A **81**, 1691 (2001).
[11] K. Gall, H. Sehitoglu, H. J. Maier, and K. Jacobus, Metall. Mater. Trans. A **29**, 765 (1998).
[12] G. R. Barsch and J. A. Krumhansl, Phys. Rev. Lett. **53**, 1069 (1984).
[13] A. E. Jacobs, Phys. Rev. B **52**, 6327 (1995).
[14] S. Kartha, J. A. Krumhansl, J. P. Sethna, and L. K. Wickham, Phys. Rev. B **52**, 803 (1995).
[15] S. R. Shenoy, T. Lookman, A. Saxena, and A. R. Bishop, Phys. Rev. B **60**, R12537 (1999).
[16] T. Lookman, S. R. Shenoy, K. Ø. Rasmussen, A. Saxena, and A. R. Bishop, Phys. Rev. B **67**, 024114 (2003).
[17] R. Ahluwalia, T. Lookman, and A. Saxena, Acta Mater. **54**, 2109 (2006).
[18] I. Groma, Phys. Rev. B **56**, 5807 (1997).
[19] I. Groma and P. Balogh, Acta Mater. **47**, 3647 (1999).
[20] B. Bakó and I. Groma, Phys. Rev. B **60**, 122 (1999).
[21] J. P. Hirth and J. Lothe, *Theory of Dislocations*, 2nd ed. (Wiley, New York, 1982).
[22] D. Hull and D. J. Bacon, *Introduction to Dislocations*, 4th ed. (Butterworth-Heinemann, Oxford, 2001).
[23] M. Peach and J. S. Koehler, Phys. Rev. **80**, 436 (1950).
[24] A. El-Azab, Modell. Simul. Mater. Sci. Eng. **8**, 37 (2000).
[25] A. El-Azab, Phys. Rev. B **61**, 11956 (2000).
[26] E. Kröner, *Continuum Theory of Dislocations and Self-Stresses* (Springer-Verlag, Berlin, 1958).
[27] M. Zaiser, M. Carmen Miguel, and I. Groma, Phys. Rev. B **64**, 224102 (2001).

[28] M. Zaiser, Adv. Phys. **55**, 185 (2006).
[29] A. M. Kosevich, Usp. Fiz. Nauk **158**, 1314 (1964).
[30] J. Kratochvíl and R. Sedláček, Phys. Rev. B **67**, 094105 (2003).
[31] R. Sedláček, C. Schwarz, J. Kratochvíl, and E. Werner, Philos. Mag. **87**, 1225 (2007).
[32] J. M. Rickman and J. Viñals, Philos. Mag. A **75**, 1251 (1997).
[33] A. Roy and A. Acharya, J. Mech. Phys. Solids **53**, 143 (2005).
[34] S. Limkumnerd and J. P. Sethna, Phys. Rev. Lett. **96**, 095503 (2006).
[35] F. C. Lovey and V. Torra, Prog. Mater. Sci. **44**, 189 (1999).
[36] D. Ríos-Jara and G. Guénin, Acta Metall. **35**, 109 (1987).
[37] J. Pons, F. C. Lovey, and E. Cesari, Acta Metall. Mater. **38**, 2733 (1990).
[38] K. Bhattacharya, S. Conti, G. Zanzotto, and J. Zimmer, Nature (London) **428**, 55 (2004).
[39] F. J. Pérez-Reche, L. Truskinovsky, and G. Zanzotto, Phys. Rev. Lett. **99**, 075501 (2007).
[40] S. Conti and G. Zanzotto, Arch. Ration. Mech. Anal. **173**, 69 (2004).
[41] A. G. Khachaturyan, *Theory of Structural Transformations in Solids* (Wiley, New York, 1983).
[42] Y. U. Wang, Y. M. Jin, A. M. Cuitiño, and A. G. Khachaturyan, Acta Mater. **49**, 1847 (2001).
[43] G. A. Malygin, Phys. Usp. **44**, 173 (2001).
[44] A. N. Gulluoglu, D. J. Srolovitz, R. LeSar, and P. S. Lomdahl, Scr. Metall. **23**, 1347 (1989).
[45] F. J. Worzala and W. H. Robinson, Philos. Mag. **15**, 939 (1967).
[46] D. Halley, Y. Samson, A. Marty, P. Bayle-Guillemaud, C. Beigné, B. Gilles, and J. E. Mazille, Phys. Rev. B **65**, 205408 (2002).
[47] E. Kröner, *Continuum Theory of Defects* (North-Holland, Amsterdam, 1981), pp. 215–315.
[48] The term "net dislocation" is used here in a loose sense and should not be thought of as a crystal dislocation. The reason is that the net Burgers vector is a vector sum of the Burgers vectors of individual crystallographic dislocations. Therefore, it can assume in general any orientation and magnitude.
[49] In the following, we will show that both elastic and plastic parts of the distortion tensor contain signatures of individual dislocations. To simplify the notation, we avoid the superscript e that often labels the elastic part of the distortion tensor.
[50] Tensorial representations of divergence, curl, and incompatibility are given in Appendix A.
[51] The Saint-Venant law is satisfied for all irrotational strain fields, such as, for example, those due to point defects.
[52] There seem to be two equivalent definitions of this tensor in the literature. In the original Kröner's formulation, $\boldsymbol{\alpha}=-\nabla\times\boldsymbol{\beta}$ and the incompatibility of strains is then defined as $\boldsymbol{\eta}=\nabla\times\boldsymbol{\varepsilon}\times\nabla$. Here, we adopt the convention of El-Azab (Ref. 24), whereby $\boldsymbol{\alpha}=\nabla\times\boldsymbol{\beta}$. This allows us to write the incompatibility constraint in a more intuitive way as $\boldsymbol{\eta}=\nabla\times\nabla\times\boldsymbol{\varepsilon}$.
[53] J. F. Nye, Acta Metall. **1**, 153 (1953).
[54] L. D. Landau and E. M. Lifshitz, *Theory of Elasticity*, 3rd ed. (Butterworths, London, 1986).
[55] A similar approach is valid also in higher dimensions, where typically more than one primary order parameter is needed to identify the phase transition.
[56] In the isotropic case, $C_{11}-C_{12}=2C_{44}$ and, therefore, only two elastic constants are independent. Hence, only two of the three coefficients A_1, A_2, and A_3 in the free energy are independent since $A_2=A_3/2$.
[57] K. Ø. Rasmussen, T. Lookman, A. Saxena, A. R. Bishop, R. C. Albers, and S. R. Shenoy, Phys. Rev. Lett. **87**, 055704 (2001).
[58] If we consider periodic boundary conditions, the integration by parts transfers the derivatives of the variations of e_1 and e_3 to the derivatives of λ; e.g., $\lambda\nabla^2\delta e_1$ becomes $(\nabla^2\lambda)\delta e_1$, etc.
[59] If the incompatibility field η_{33} vanishes, i.e., the medium is dislocation-free, and no external stress is applied, only the first term in Eq. (18) remains. In this case, one obtains (Ref. 14) that e_1 and e_3 can be expressed as functionals of the primary order parameter e_2 only.
[60] It is always possible to augment this deterministic relaxational dynamics by a stochastic term that is often characterized (Ref. 64) as white noise with zero mean and variance $2\Gamma k_B T$. However, it can be shown that this noise plays an important role only at the temperatures slightly below T_c, where thermal fluctuations may overcome the energy barrier between the two variants of the martensite and, therefore, cause switching between these variants. In this case, the twin boundary between individual martensite variants would not be sharp but rather diffuse. At low temperatures, i.e., well below T_c, this barrier is large and the weak thermal fluctuations cannot cause this switching. Similarly, above T_c, the free energy has one minimum corresponding to $e_2=0$ and the thermal fluctuations would merely cause broadening of the distribution of e_2. The goal of this paper is to give a proof of the principle and, for simplicity, the effect of thermal noise is not included.
[61] S. Muto, R. Oshima, and F. E. Fujita, Acta Metall. Mater. **38**, 685 (1990).
[62] B. B. van Aken, J. P. Rivera, H. Schmid, and M. Fiebig, Nature (London) **449**, 702 (2007).
[63] D. S. Chandrasekharaiah and L. Debnath, *Continuum Mechanics* (Academic, New York, 1994).
[64] F. Sagués, J. M. Sancho, and J. García-Ojavlo, Rev. Mod. Phys. **79**, 829 (2007).